# Dynamic tunable LWIR achromatic metalens comprising all-$As_2Se_3$ microstructures

**Zhihao He (贺志豪)[1], Bingxia Wang (王炳霞)[1,*], Zhiang Qian (钱志昂)[1], Kongsi Zhou(周孔思)[1], Xiang Shen (沈祥)[1] and Yungui Ma (马云贵)[2]**

[1]Laboratory of Infrared Materials and Devices, Research Institute of Advanced Technologies, Key Laboratory of Photoelectric Detection Materials and Devices of Zhejiang Province, Ningbo University, China

[2]State Key Lab of Modern Optical Instrumentation, Centre for Optical and Electromagnetic Research, College of Optical Science and Engineering, International Research Center for Advanced Photonics, Zhejiang University, China
*Corresponding author: wangbingxia@nbu.edu.cn

Received Month X, XXXX; accepted Month X, XXXX; posted online Month X, XXXX

In the field of long-wave infrared (LWIR) thermal imaging, vital for applications such as military surveillance and medical diagnostics, metalenses show immense potential for compact, lightweight, and low-power optical systems. However, to date, the development of LWIR broadband achromatic metalenses with dynamic tunable focus, which are suitable for both coaxial and off-axis applications, remains a largely unexplored area. Herein, we have developed an extensive database of broadband achromatic all-$As_2Se_3$ microstructure units for the LWIR range. Utilizing this database with the Particle Swarm Optimization (PSO) algorithm, we have designed and demonstrated LWIR broadband achromatic metalenses capable of coaxial and off-axis focusing with three dynamic tunable states. This research may have potential applications for the design of compact, high-performance optical devices, including those with extreme depth-of-field and wide-angle imaging capabilities.

**Keywords***:* Achromatic metalens; Long-wave infrared (LWIR); Dynamic tunable focus.
DOI: 10.3788/COLXXXXXX.XXXXXX.

## 1. Introduction

Long-wave infrared (LWIR) thermal imaging, capable of providing critical information in scenarios where traditional visual observation is not sufficient, is of great significance in fields such as night vision, medical diagnosis, and aerospace [1-3]. The focus on Size, Weight, Power, Price, and Performance (SWaP3) optimization in LWIR thermal imaging systems is a key trend in research and development. Metalenses, capable of their subwavelength scale manipulation of wavefront information such as amplitude, phase, and polarization, mark a significant advancement in optical technology [4-10]. They offer the potential to replace or supplement traditional lenses in applications requiring high precision imaging or in miniature optical systems, attracting significant attention recently.

In 2011, the Capasso group at Harvard University first proposed the concept of metasurface with anomalous reflection and refraction [11]. Following this, in 2012, a seminal paper on metalenses was published, showcasing the remarkable ability of metalenses to manipulate light at subwavelength scales [12]. In the past decade, great efforts have been made to develop high-efficiency [13-15], achromatic [16,17], and aberration-corrected [18,19] metalenses. Currently, a range of multifunctional imaging techniques and highly integrated devices utilizing metalenses have been developed, particularly in the visible spectrum. Techniques such as spectral tomographic imaging[ 20], spiral phase contrast imaging [21], extreme depth-of-field imaging [22], spectral light-field imaging [9], and planar wide-angle imaging [23] demonstrate the versatility of metalenses. Moreover, highly integrated devices like metalens endoscopes [24], phase gradient microscopy [25], polarization cameras [26], and pancake meta-optics cameras [27] showcase the broad application prospects of metalens technology. In recent years, LWIR metalenses have shown significant progress, particularly in wide field-of-view imaging [28-32], and broadband achromatic imaging [33-40]. However, to date, the development of LWIR broadband achromatic metalenses with dynamically tunable focus, which are suitable for both coaxial and off-axis applications, remains an important area of research.

In this work, we focus on developing a database of achromatic microstructure units and utilize the PSO algorithm for the design of dynamic tunable LWIR broadband achromatic metalenses. Given that Si and Ge, commonly used in LWIR metalenses, encounter issues like high refractive indices leading to significant reflection losses and inherent absorption in the LWIR band [41-42], $As_2Se_3$ presents a favorable alternative. It boasts a lower refractive index, approximately 2.78 at the LWIR range, and a lower refractive index temperature coefficient, effectively reducing losses and bolstering temperature stability [43]. Moreover, the compatibility of $As_2Se_3$ with CMOS processes [44] significantly strengthens its applicability in LWIR metalens applications. These properties of As2Se3 not only improve focusing efficiency and temperature stability, but also open up new possibilities for advanced LWIR imaging solutions. Therefore, we employed annular and circular cylindrical microstructures on $As_2Se_3$ glass to build the all-$As_2Se_3$ microstructure units database. The designed LWIR achromatic metalens comprising all-$As_2Se_3$ microstructure

units are composed of two parts: a central sub-metalens for near-distance focusing and an outer annular sub-metalens for far-distance focusing. By altering the illumination area, dynamic control of coaxial and off-axis focusing with three dynamic tunable states can be achieved. This work may have potential applications in the design of compact and high-performance optical devices.

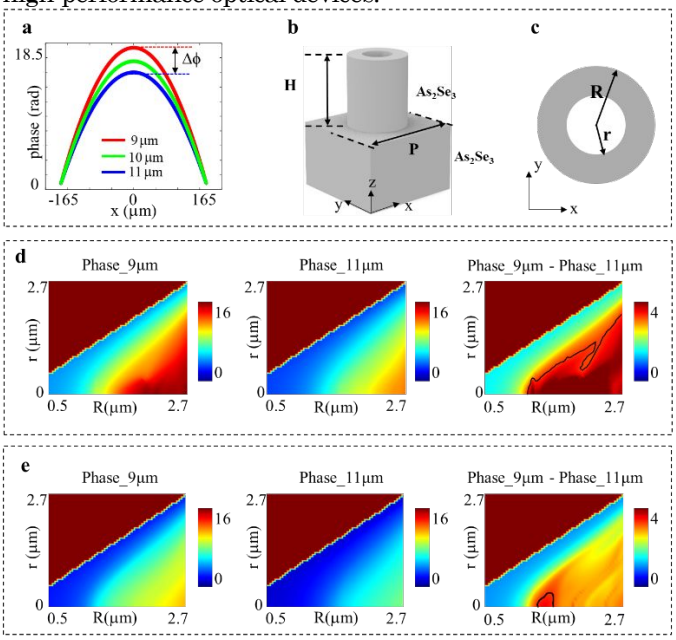


**Fig. 1.** Database of all-$As_2Se_3$ microstructure units designed for the 9-11 μm wavelength range. (a) The ideal phase profile of a broadband achromatic metalens for wavelengths λ = 9μm, 10μm, 11μm. (b-c) Microstructure unit. (d) Dispersion compensation ability of microstructure units database with a height of 11μm. (e) Dispersion compensation ability of microstructure units database with a height of 8μm.

## 2. Principle and Design

The design and illustration of an extensive database for constructing a broadband achromatic single-layer all-$As_2Se_3$ metalens, specifically targeting the 9-11 μm wavelength range, is depicted in Fig. 1. Fig. 1(a) displays the ideal phase profile for an achromatic metalens with an aperture of 330 μm and a focal length of 500 μm at wavelengths λ = 9μm, 10μm, 11 μm. The maximum phase difference across these wavelengths, Δϕ, is 3.4 rad. This spatial phase distribution, which depends on the incident wavelength, can be achieved in principle by subwavelength units of different topologies and structural parameters. In this work, as shown in Fig. 1(b, c), microstructures made of subwavelength $As_2Se_3$ annular cylinder (r>0) or circular cylinder (r=0) on $As_2Se_3$ substrates are employed. The structural parameters of each antenna are as follows: outer radius (R); inner radius (r); height (H); and period (P). In the design of achromatic metalenses, an increased height is beneficial for better dispersion compensation. Therefore, calibrating the microstructure height to align with the designated achromatic wavelength range is a fundamental way to improve optimal performance. Fig. 1(d) displays the dispersion compensation ability of microstructure units with a height (H) of 11 μm when the period (P) is 5.5 μm. The phase of the transmitted electric field versus the outer radius (R) and the inner radius (r) at different incident wavelengths of 9 μm and 11 μm are shown in Fig. 1(d) (left, middle). Fig. 1(d) (right) represents the difference between the phases at 9 μm and 11 μm incident wavelengths, indicating the dispersion compensation capability of the 11-μm high microstructure units database. The black solid line in Fig. 1(d) (right) represents the contour line at a phase compensation value of Δφ=3.4 rad, showing the number of microstructures with phase compensation values below 3.4 rad is relatively limited, thus not fulfilling the criteria for database inclusion. Fig. 1(e) displays the dispersion compensation ability of the microstructure units database with a height (H) of 8 μm when the period (P) is 5.5 μm. The phase of the transmitted electric field versus the outer radius (R) and the inner radius (r) at different incident wavelengths of 9 μm and 11 μm are shown in Fig. 1(e) (left, middle). Fig. 1(e) (right) represents the difference between the phases at 9 μm and 11 μm incident wavelengths, indicating the dispersion compensation capability of the 8-μm high microstructure units database. The black solid line in Fig. 1(e) (right) represents the contour line at a phase compensation value of Δφ=3.4 rad, showing the number of microstructures with phase compensation values below 3.4 rad is sufficient, thus fulfilling the criteria for database inclusion. Herein we fixed the height (H) at 8 μm and constructed the database of broadband achromatic microstructures for the 9-11 μm wavelength range by varying the outer radius (R) and inner radius (r).

## 3. Results and Discussion

To verify the chromatic correction capability of the developed all-$As_2Se_3$ microstructure units database, in this section, we utilize this database combined with the PSO algorithm to design an achromatic metalens. The schematic diagram illustrating achromatic focusing is shown in Fig. 2(a). The theoretical phase distribution and realized phase distribution with the PSO algorithm at different wavelengths for a fixed focal length (f=500μm) are shown by the blue curves and red dots in Fig. S1 (Supporting Information). The structural parameter and transmittance of the microstructures composing the achromatic metalens are shown in Fig. S2 (Supporting Information). The designed achromatic metalens and an expanded view of the microstructure arrays in the marked area are shown in Fig. 2(b). The output electric field from the achromatic metalens was numerically calculated using finite-difference time-domain (FDTD) simulation software for normal plane-wave incidence. The intensity evolution along the z-axis is shown in the first row in Fig. 2(c). The focal length remains almost constant when the incident wavelength changes, indicating the realization of a broadband achromatic focusing in the LWIR region. The second row in Fig. 2(c) shows the electric field intensity distributions at the focal plane (z = 500 μm), and the green

line represents the intensity distribution at y =0 μm. To further examine the focusing performance of designed achromatic metalens, full-width at half-maximum (FWHM) and focusing efficiency across five wavelengths for the achromatic metalens are calculated, as shown in Fig. S3 (Supporting Information). As a comparison, the focusing performance of chromatic metalens without PSO algorithm optimization at different wavelengths is shown in Fig. 2(d).

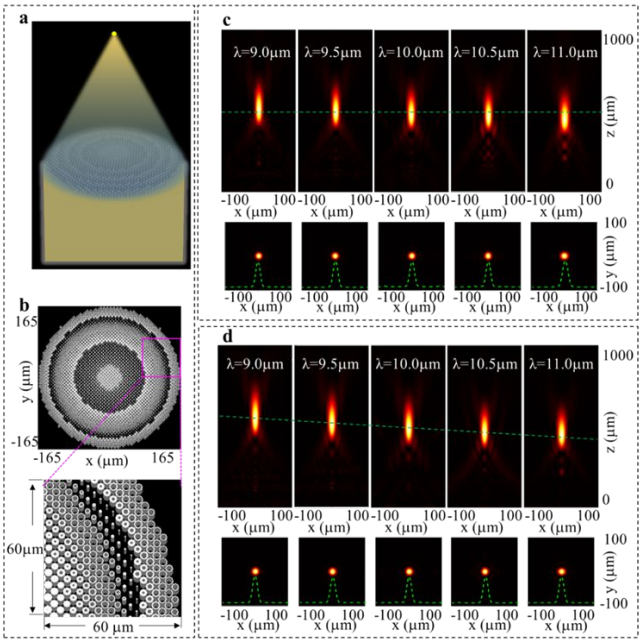


**Fig. 2.** Design and focusing performance of an LWIR broadband achromatic all-$As_2Se_3$ metalens. (a) Schematic diagram illustrating achromatic focusing. (b) The designed achromatic metalens and an expanded view of the microstructure arrays in the marked area. (c) Intensity profiles of achromatic metalens along axial planes at various incident wavelengths. (d). Intensity profiles of chromatic metalens without PSO algorithm optimization.

After confirming the chromatic correction capability of the all-$As_2Se_3$ microstructure units database, we now use this database to design an achromatic metalens with dynamic tunable coaxial focusing capability. The schematic diagram illustrating an achromatic coaxial tunable focusing under different incident light illumination areas is shown in Fig. 3(a). The all-$As_2Se_3$ achromatic metalens is composed of two parts: a central circular sub-metalens in the central area, designed for encoding the phase for near-distance focusing with focal lengths $f_1$ = 500 μm, and a sub-metalens in the outer annular region, designed for encoding the phase for far-distant focusing with focal lengths $f_2$ = 900 μm. The theoretical phase distribution and realized phase distribution with the PSO algorithm at different wavelengths are shown by the blue curves and red dots in Fig. S4 (Supporting Information). The structural parameter and transmittance of the microstructures composing the achromatic metalens are shown in Fig. S5 (Supporting Information). The designed achromatic metalens and an expanded view of the microstructure arrays in the marked area are shown in Fig. 3(b). The dynamic focusing capability of the metalens under varying incident light illumination areas at different wavelengths is illustrated in Fig. 3(c). Specifically, each row in the figure represents a distinct focusing state: the first row shows near-distance focusing (State 1) achieved by illuminating the metalens's inner circular area; the second row displays far-distance focusing (State 2) by illuminating its outer annular region; and the third row demonstrates near-far bifocal focusing (State 3) achieved by illuminating the entire metalens. Additionally, each column corresponds to the dynamic control of these three focusing states across five different wavelengths: 9.0 μm, 9.5 μm, 10.0 μm, 10.5 μm, and 11.0 μm, respectively. The focal length in each focus state remains almost constant when the incident wavelength changes, indicating broadband achromatic focusing. The insets in Fig. 3(c) show the corresponding electric field intensity distributions at the focal plane. To further examine the focusing performance of designed achromatic metalens, we define the focusing efficiency as the ratio between the integral of electric field intensity within a focal plane diameter D region and the electric field intensity's integral at the metalens's output surface. Then, the focusing efficiency for these three states can be written as $\eta_1=\frac{\sum_D I_{f1}}{\sum_{S1} I}$, $\eta_2=\frac{\sum_D I_{f2}}{\sum_{S2} I_{total}}$, $\eta_3=\frac{\sum_D I_{f1}}{\sum_{S1+S2} I}+\frac{\sum_D I_{f2}}{\sum_{S1+S2} I}$, where D is three times the FWHM, and (S1, S2) represent the areas of the two sub-metaleenses. FWHM and focusing efficiency of the achromatic metalens for three states are characterized, as shown in Fig. S6 (Supporting Information).

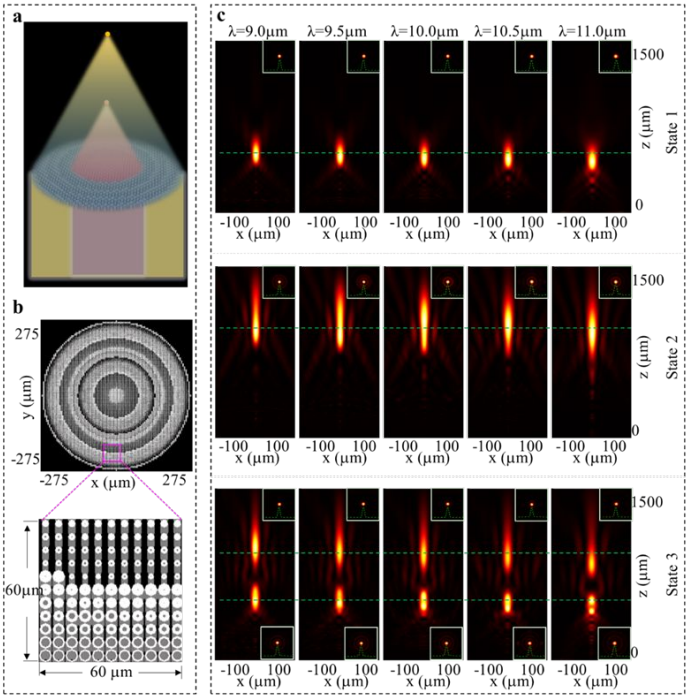

**Fig. 3.** Design and dynamic coaxial focusing performance of an LWIR broadband achromatic all-$As_2Se_3$ metalens. (a) Schematic diagram demonstrating dynamic tunable coaxial focusing. (b) The designed achromatic metalens with an expanded view of the microstructure arrays in the marked area. (c) Intensity evolution of each focusing state along the z-axis.

After demonstrating the dynamic tunable coaxial focusing with the designed achromatic metalens, we now aim to adapt this technology for off-axial focusing. The schematic diagram illustrating an achromatic off-axial tunable focusing under different incident light illumination areas is shown in Fig. 4(a). The all-$As_2Se_3$ achromatic metalens is composed of two parts: a central circular sub-metalens with a phase gradient of $\pi/22$ rad $\mu m^{-1}$ for near-distance right-deflection focusing with focal length $f_1$ = 500 μm, and an outer annular sub-metalens with a phase gradient of $-\pi/22$ rad $\mu m^{-1}$ for far-distant left-deflection focusing with focal length $f_2$ = 900 μm. The theoretical phase distribution and realized phase distribution with the PSO algorithm at different wavelengths are shown by the blue curves and red dots in Fig. S7 (Supporting Information). The structural parameter and transmittance of the microstructures composing the achromatic metalens are shown in Fig. S8 (Supporting Information). The designed achromatic metalens and an expanded view of the microstructure arrays in the marked area are shown in Fig.4(b). The dynamic focusing capability of the metalens under varying incident light illumination areas at different wavelengths is depicted in Fig. 4(c). Specifically, each row in the figure represents a distinct focusing state: the first row shows near-distance right-deflection focusing (State 1) achieved by illuminating the metalens's inner circular area; the second row displays far-distance left-deflection focusing (State 2) by illuminating its outer annular region; and the third row demonstrates near-far bifocal focusing (State 3) achieved by illuminating the entire metalens. Additionally, each column corresponds to the dynamic control of these three focusing states across five different wavelengths: 9.0 μm, 9.5 μm, 10.0 μm, 10.5 μm, and 11.0 μm, respectively. The focal length in each focus state remains almost constant when the incident wavelength changes, indicating broadband achromatic focusing. The insets in Fig. 4(c) show the corresponding electric field intensity distributions at the focal plane. To further examine the focusing performance of designed achromatic metalens, FWHM and focusing efficiency of the achromatic metalens for three states are featured, as shown in Fig. S9 (Supporting Information).

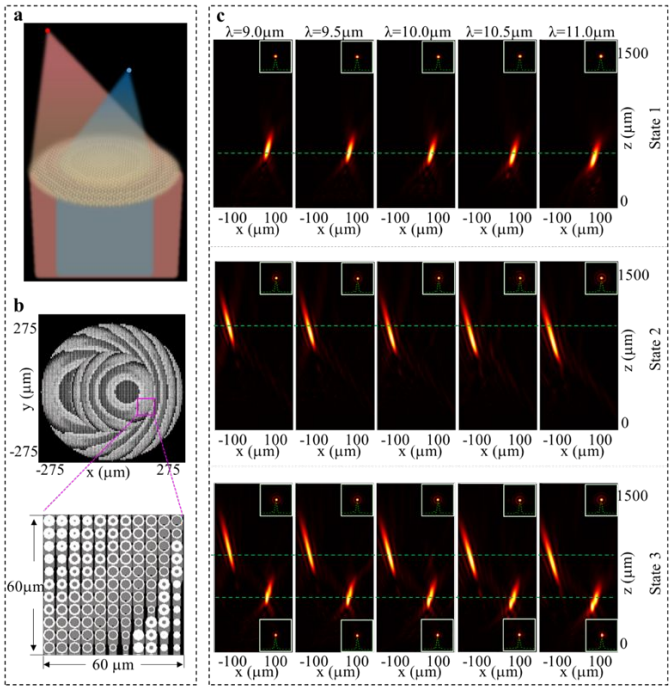


**Fig. 4.** Design and dynamic off-axial focusing performance of an LWIR broadband achromatic all-$As_2Se_3$ metalens. (a) Schematic diagram demonstrating the dynamic off-axial focusing. (b) The designed achromatic metalens with an expanded view of the microstructure arrays in the marked area. (c) Intensity evolution of each focusing state along the z-axis.

## 4. Conclusion

In conclusion, we developed an extensive database of broadband achromatic all-$As_2Se_3$ microstructures for the LWIR spectrum. The chromatic correction capability of the developed dataset was verified by constructing an LWIR broadband achromatic metalens with a fixed focus. This type of LWIR achromatic metalens can be utilized in scenarios that demand high precision imaging yet require compact optical systems, such as drones and personal portable Night Vision Goggles. Furthermore, using this developed database in conjunction with the PSO algorithm, LWIR metalenses capable of achromatic focusing with three dynamically tunable states, suitable for both coaxial and off-axis focusing, were achieved. This proposed multi-focus metalens is capable of imaging targets at various distances and angles, offering significant utility in scenarios requiring precise imaging across different depths and perspectives, such as obstacle detection and avoidance in autonomous vehicles, navigation of robots in complex environments, detailed observation in medical tomography, and accurate data collection in environmental monitoring and terrain mapping. This study provides a way to realize multifunctional LWIR broadband achromatic metalenses, which may offer the potential for the development of multifunctional LWIR achromatic metalenses with capabilities such as enhanced depth of field and wide field-of-view.

Acknowledgment

This work is supported by National Natural Science Foundation of China (Grant No. 62105171), Zhejiang Provincial Natural Science Foundation of China under Grant No. LY24F050001 Joint Funds of the National Natural Science Foundation of China (U21A2056); Key Research and Development program of Zhejiang Province (2021C01025); K. C. Wong Magna Fund in Ningbo University.

## References References

1. D. Ren, C. Dong, S. J. Addamane, et al., "High-quality microresonators in the longwave infrared based on native germanium," Nat. Commun. **13**(1), 5727 (2022).
2. T. S. Kleine, T. Lee, K. J. Carothers, et al., "Infrared Fingerprint Engineering: A Molecular-Design Approach to Long-Wave Infrared Transparency with Polymeric Materials," Angew. Chem. **58**(49), 17656-17660 (2019).
3. M. Meem, S. Banerji, A. Majumder, et al., "Broadband lightweight flat lenses for long-wave infrared imaging," PNAS **116**(43), 21375-21378 (2019).
4. L. Li, Z. Liu, X. Ren, et al., "Metalens-array–based high-dimensional and multiphoton quantum source," Science **368**(6498), 1487-1490 (2020).
5. X. Zou, R. Lin, Y. Fu, et al., "Advanced Optical Imaging Based on Metasurfaces," Adv. Optical Mater., 2203149 (2023).
6. X. Zou, Y. Zhang, R. Lin, et al., "Pixel-level Bayer-type colour router based on metasurfaces," Nat. Commun. **13**(1), 3288 (2022).
7. B. Wang, K. Wang, X. Hong, et al., "Resonant nonlinear synthetic metasurface with combined phase and amplitude modulations," Laser & Photon. Rev. **15**(7), 2100031 (2021).
8. X. Zhou, and S. Wang, "Class-specific diffractive cameras based on deep learning-designed surfaces," Light: Science & Applications **11**(1), 283 (2022).
9. X. Hua, Y. Wang, S. Wang, et al., "Ultra-compact snapshot spectral light-field imaging," Nat. Commun. **13**(1), 2732 (2022).
10. K. Zhou, B. Wang, S. Tang, et al., "Mid-infrared biomimetic moth-eye-shaped polarization-maintaining and angle-insensitive metalens," Opt. Express **30**(7), 12048-12060 (2022).
11. N. Yu, P. Genevet, M. A. Kats, et al., "Light propagation with phase discontinuities: Generalized laws of reflection and refraction," Science **334**(6054), 333-337 (2011).
12. F. Aieta, P. Genevet, M. A. Kats, et al., "Aberration-free ultrathin flat lenses and axicons at telecom wavelengths based on plasmonic metasurfaces," Nano Lett. **12**(9), 4932-4936 (2012).
13. S. Zhang, M.-H. Kim, F. Aieta, et al., "High efficiency near diffraction-limited mid-infrared flat lenses based on metasurface reflectarrays," Opt. Express **24**(16), 18024-18034 (2016).
14. A. Arbabi, Y. Horie, A. J. Ball, et al., "Subwavelength-thick lenses with high numerical apertures and large efficiency based on high-contrast transmitarrays," Nat. Commun. 6, 7069 (2015).
15. S. Zeng, S. Pian, M. Su, et al., "Hierarchical-morphology metafabric for scalable passive daytime radiative cooling," Science 373(6555), 692-696 (2021).
16. S. Wang, P. C. Wu, V. C. Su, et al., "Broadband achromatic optical metasurface devices," Nat. Commun. **8**, 187 (2017).
17. Q. Chen, Y. Gao, S. Pian, et al., "Theory and Fundamental Limit of Quasiachromatic Metalens by Phase Delay Extension," Phys. Rev. Lett. **131**(19), 193801 (2023).
18. A. Arbabi, E. Arbabi, S. M. Kamali, et al., "Miniature optical planar camera based on a wide-angle metasurface doublet corrected for monochromatic aberrations," Nat. Commun. **7**(1), 13682 (2016).
19. B. Groever, W. T. Chen, and F. Capasso, "Meta-Lens Doublet in the Visible Region," Nano Lett. **17**(8), 4902-4907 (2017).
20. C. Chen, W. Song, J.-W. Chen, et al., "Spectral tomographic imaging with aplanatic metalens," Light: Science & Applications **8**, 99 (2019).
21. P. Huo, C. Zhang, W. Zhu, et al., "Photonic Spin-Multiplexing Metasurface for Switchable Spiral Phase Contrast Imaging," Nano Lett. **20**(4), 2791-2798 (2020).
22. Q. Fan, W. Xu, X. Hu, et al., "Trilobite-inspired neural nanophotonic light-field camera with extreme depth-of-field," Nat. Commun. **13**(1), 2130 (2022).
23. J. Chen, X. Ye, S. Gao, et al., "Planar wide-angle-imaging camera enabled by metalens array," Optica **9**(4), 431-437 (2022).
24. H. Pahlevaninezhad, M. Khorasaninejad, Y.-W. Huang, et al., "Nano-optic endoscope for high-resolution optical coherence tomography in vivo," Nat. Photonics **12**(9), 540-547 (2018).
25. H. Kwon, E. Arbabi, S. M. Kamali, et al., "Single-shot quantitative phase gradient microscopy using a system of multifunctional metasurfaces," Nat. Photonics **14**(2), 109-114 (2020).
26. N. A. Rubin, G. D'Aversa, P. Chevalier, et al., "Matrix Fourier optics enables a compact full-Stokes polarization camera," Science **365**(6448), 43 (2019).
27. C. Chen, X. Ye, J. Sun, et al., "Bifacial-metasurface-enabled pancake metalens with polarized space folding," Optica **9**(12), 1314-1322 (2022).
28. Y. Wang, S. Zhang, M. Liu, et al., "Compact meta-optics infrared camera based on a polarization-insensitive metalens with a large field of view," Opt. Lett. **48**(17), 4709-4712 (2023).
29. Q. Fan, M. Liu, C. Yang, et al., "A high numerical aperture, polarization-insensitive metalens for long-wavelength infrared imaging," Appl. Phys. Lett. **113**(20), 201104 (2018).
30. S. Shrestha, A.C. Overvig, M. Lu, et al., "Broadband achromatic dielectric metalenses," Light: Science & Applications **7**, 85 (2018).
31. J. Li, Y. Wang, S. Liu, et al., "Largest aperture metalens of high numerical aperture and polarization independence for long-wavelength infrared imaging," Opt. Express **30**(16), 28882-28891 (2022).
32. A. Wirth-Singh, J. E. Fröch, Z. Han, et al., "Large field-of-view thermal imaging via all-silicon meta-optics," Appl. Opt. **62**(20), 5467-5474 (2023).
33. S. Yue, Y. Liu, R. Wang, et al., "All-silicon polarization-independent broadband achromatic metalens designed for the mid-wave and long-wave infrared," Opt. Express **31**(26), 44340-44352 (2023).
34. V. Saragadam, Z. Han, V. Boominathan, et al., "Foveated thermal computational imaging prototype using all-silicon meta-optics," Optica **11**(1), 18-25 (2024).
35. N. Song, N. Xu, D. Shan, et al., Broadband Achromatic Metasurfaces for Longwave Infrared Applications. In *Nanomaterials*, 2021; Vol. 11, p 2760.
36. D. Shan, N. Xu, J. Gao, et al., "Design of the all-silicon long-wavelength infrared achromatic metalens based on deep silicon etching," Opt. Express **30**(8), 13616-13629 (2022).
37. C. Xia, M. Liu, J. Wang, et al., "A polarization-insensitive infrared broadband achromatic metalens consisting of all-silicon anisotropic microstructures," Appl. Phys. Lett. **121**(16), 161701 (2022).

38. N. Song, N. Xu, J. Gao, et al., "Broadband Achromatic and Polarization Insensitive Focused Optical Vortex Generator Based on Metasurface Consisting of Anisotropic Nanostructures," Frontiers in Physics **10**(1), 846718 (2022).
39. L.-R. Zhao, X.-Q. Jiang, C.-X. Li, et al., "High-NA and broadband achromatic metalens for sub-diffraction focusing of long-wavelength infrared waves," Results in Physics **46**, 106308 (2023).
40. Y. Zheng, S. Zheng, Y. Dong, et al., "Broadband Achromatic Metalens in the Long-Wave Infrared Regime," IEEE Photonics Journal **15**(2), 1-7 (2023).
41. H. W. Icenogle, B. C. Platt, and W. L. Wolfe, "Refractive indexes and temperature coefficients of germanium and silicon," Appl. Opt. **15**(10), 2348-2351 (1976).
42. I. A. Kaplunov, Y. M. Smirnov, and A. I. Kolesnikov, "Optical transparency of crystalline germanium," J. Opt. Technol. **72**(2), 214-220 (2005).
43. www.ir-glass.com/usr/uploads/2018/02/1392963412.pdf.
44. B. J. Eggleton, B. Luther-Davies, and K. Richardson, "Chalcogenide photonics," Nat. Photonics **5**(3), 141-148 (2011).